

# Evidence for H<sub>2</sub>-Induced Ductility in a Pt/Al<sub>2</sub>O<sub>3</sub> Catalyst

Eleonora Vottero,\* Michele Carosso, Alberto Ricchebuono, Monica Jiménez-Ruiz, Riccardo Pellegrini, Céline Chizallet, Pascal Raybaud, Elena Groppo, and Andrea Piovano



Cite This: *ACS Catal.* 2022, 12, 5979–5989



Read Online

ACCESS |



Metrics & More



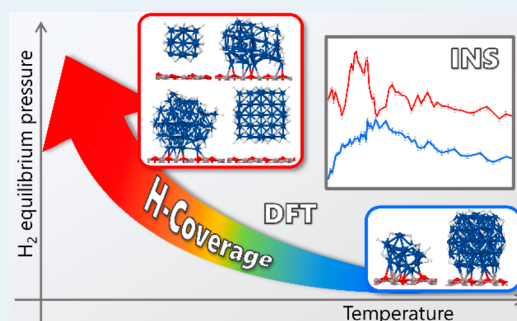
Article Recommendations



Supporting Information

**ABSTRACT:** Focusing on a highly dispersed 5 wt % Pt/Al<sub>2</sub>O<sub>3</sub> catalyst for industrial hydrogenation and dehydrogenation reactions, we employ inelastic neutron scattering (INS) spectroscopy to obtain the vibrational fingerprint of the hydrogenous species formed under different H<sub>2</sub> equilibrium pressure and temperature. The INS profiles are interpreted on the basis of systematic DFT simulations on 26 different Pt<sub>x</sub>H<sub>y</sub>/γ-Al<sub>2</sub>O<sub>3</sub> models, indicating that the INS spectra are a unique fingerprint of the Pt<sub>x</sub>H<sub>y</sub>/γ-Al<sub>2</sub>O<sub>3</sub> model morphology, size (*x*), H-coverage (*y*), and typology of Pt–H species. We fit the experimental INS spectrum of Pt/Al<sub>2</sub>O<sub>3</sub> measured under higher H-coverage conditions with a linear combination of the simulated spectra. We find that 47% of the spectrum can be ascribed to Pt<sub>55</sub>H<sub>7</sub>/γ-Al<sub>2</sub>O<sub>3</sub> clusters completely solvated by H atoms (*y* = 81 and 91) and in weak interaction with the support, followed by the disordered Pt<sub>34</sub>H<sub>54</sub>/γ-Al<sub>2</sub>O<sub>3</sub> model (36%) and by the smaller Pt<sub>13</sub>H<sub>32</sub>/γ-Al<sub>2</sub>O<sub>3</sub> one (18%). These results are in good agreement with the particle size distribution previously determined by TEM and confirmed by XAS. A second INS spectrum collected under lower H-coverage conditions exhibits the typical features of less hydrogenated Pt<sub>x</sub>H<sub>y</sub> models in stronger interaction with the γ-Al<sub>2</sub>O<sub>3</sub> support, as well as bands associated with the formation of –OH species at the support by H-spillover. Overall, our study reveals the relevance of combined INS and DFT analysis to quantify the versatile atomic scale's properties of Pt/Al<sub>2</sub>O<sub>3</sub> catalyst in terms of cluster morphology, size, typology of Pt–H species, and cluster/support interaction depending on the H-coverage, providing important insights about their behavior under hydrogenation conditions.

**KEYWORDS:** platinum nanoparticles, hydrogenation, inelastic neutron scattering, density functional theory, nanoparticles ductility



## 1. INTRODUCTION

Heterogeneous catalysts based on supported platinum nanoparticles are pivotal in the production process of many fine and bulk chemicals, including the catalytic reforming of gasoline,<sup>1,2</sup> the hydrogenation and dehydrogenation of organic substrates<sup>3–7</sup> or the oxidation of hydrocarbons and CO,<sup>8–10</sup> and also for their applications in fuel cells<sup>11</sup> or in the purification of exhaust gases.<sup>12,13</sup> The exceptional catalytic activity of platinum for hydrogenation reactions relies on its ability to activate and dissociate the H<sub>2</sub> molecule with the subsequent formation of surface platinum hydride species, which are those involved in the hydrogenation of the substrate. Although platinum has been employed in such catalytic processes since the onset of heterogeneous catalysis, many features such as the nature of the Pt–H species, the Pt–H stoichiometry,<sup>14–16</sup> their behavior under reaction conditions, the influence of the support, or the identification of the most active species in a given reaction are not yet fully understood, stimulating further investigations, which are not only of academic interest but also relevant for industrial applications.<sup>17,18</sup>

Experimental and theoretical evidence pointing out the ductility of supported Pt nanoparticles (i.e., their tendency to undergo a structural reconstruction, as a consequence of the

ability of the material to deform without breaking) as a function of reaction conditions such as the temperature and the H<sub>2</sub> partial pressure are accumulating over the years. The matter was largely addressed by means of density functional theory (DFT) simulations in refs 19 and 20, in which the most stable structures for Pt<sub>13</sub> nanoclusters on γ-Al<sub>2</sub>O<sub>3</sub> surfaces under different temperatures and equilibrium H<sub>2</sub> pressures (*P*(H<sub>2</sub>)<sub>eq</sub>) were investigated by means of *ab initio* molecular dynamics. The simulations performed on dehydrated γ-Al<sub>2</sub>O<sub>3</sub> surface models<sup>19</sup> indicated that high temperature and low *P*(H<sub>2</sub>)<sub>eq</sub> favor a biplanar geometry strongly anchored to the support, while a decrease in the temperature and/or an increase of *P*(H<sub>2</sub>)<sub>eq</sub> trigger a morphological reconstruction to a cuboctahedral Pt cluster which, eventually, get completely solvated by H atoms weakening the interaction with the support. Concomitantly with the reconstruction from a

**Received:** February 4, 2022

**Revised:** March 19, 2022

**Published:** May 6, 2022



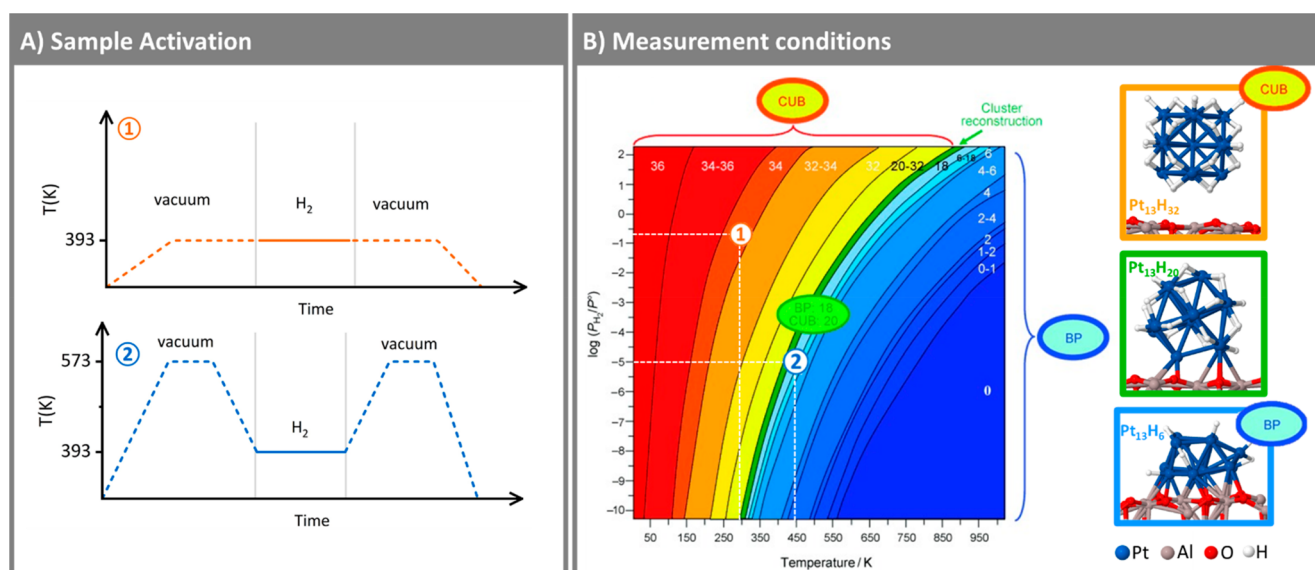


**Figure 1.** (A) Schematic description of the catalyst activation procedure prior the INS measurements for experiments (1) and (2). (B) Thermodynamic diagram displaying the most stable morphology and H-coverage for Pt<sub>13</sub>/γ-Al<sub>2</sub>O<sub>3</sub>(100) models as a function of the temperature and of the  $P(\text{H}_2)_{\text{eq}}$  as calculated in ref 19. Representative geometries for the biplanar (BP), reconstructing and cuboctahedric (CUB) geometries are shown. Circles (1) and (2) indicate the temperature and  $P(\text{H}_2)_{\text{eq}}$  at which H<sub>2</sub> was dosed during the first and second experiment. Adapted with permission from ref 19. Copyright 2011 Wiley-VCH.

bipolar to a cuboctahedric structure, a conversion of top Pt–H species (in which H is bonded to a single Pt atom) into multifolded Pt–H species was also predicted. This interconversion between top and multibridged Pt–H species and the ductility of supported Pt nanoparticles in the presence of H<sub>2</sub> was also pointed out by other computational studies on Pt<sub>x</sub> nanoparticles ( $x$  up to 44) also considering isolated clusters or other supports.<sup>21–25</sup>

Experimental evidence is also cumulating, with several instances provided by Fourier Transform Infrared spectroscopy (FT-IR),<sup>26</sup> X-ray absorption spectroscopy (XAS),<sup>20,26,27</sup> transmission electron microscopy (TEM),<sup>28</sup> or H<sub>2</sub> temperature-programmed desorption (H<sub>2</sub>-TPD).<sup>29</sup> In this respect, some of us have recently investigated the modifications undergone by a Pt/Al<sub>2</sub>O<sub>3</sub> catalyst when varying the hydrogenation conditions by simultaneous XAS-DRIFT-MS measurements performed under *operando* conditions.<sup>26</sup> When reducing the H<sub>2</sub> concentration, a progressive modification of the coordination number and of the Pt–Pt bond distances was observed, indicating the occurrence of a structural change in the Pt nanoparticles. Four different top Pt–H species were detected at the Pt nanoparticles surface, whose amount initially increased when reducing the H<sub>2</sub> concentration up to a maximum, after which they completely disappeared. This counterintuitive behavior was attributed to the conversion of multifolded Pt–H species (not visible by IR techniques because they are obscured by the intense vibrational modes of the Al<sub>2</sub>O<sub>3</sub> support) into top ones (which instead are detected by IR), as predicted by DFT calculations.

To access the complete vibrational spectrum of Pt–H species, inelastic neutron scattering (INS) spectroscopy coupled with advanced DFT simulations is mandatory.<sup>30–32</sup> This method is well-known for providing detailed information about all the H-containing species in several classes of samples<sup>33</sup> in the form of vibrational spectra. This is possible thanks to the lightweight and the high neutron scattering cross-section of <sup>1</sup>H nuclei, as well as to the absence of selection rules,

which make INS particularly sensitive toward all the vibrational modes involving H atoms. The potential of this coupled approach was recently shown in the work of Parker et al.,<sup>34</sup> who compared the INS spectrum of an unsupported Pt<sub>44</sub>H<sub>80</sub> tetradecahedron model with the experimental spectra of hydrogen on Pt black and of a few Pt-based catalysts on different supports and with different metal loading and particle size. However, the effects of the support and of the Pt nanoparticle size, shape, and the H-coverage were never systematically investigated either computationally or experimentally. In the present work, we systematically simulated the INS spectra of a large pool of Pt<sub>x</sub>H<sub>y</sub>/γ-Al<sub>2</sub>O<sub>3</sub> models (13 ≤  $x$  ≤ 55), and we compared them with the experimental INS spectra of a highly dispersed Pt/Al<sub>2</sub>O<sub>3</sub> catalyst under two markedly different H-coverage conditions. We obtained a complete description of the H<sub>2</sub>-induced dynamics of Al<sub>2</sub>O<sub>3</sub>-supported Pt nanoparticles as a function of the temperature and of the  $P(\text{H}_2)_{\text{eq}}$ , pointing out details concerning the H atoms' coordination mode, the Pt clusters morphology and size, as well as the impact of the support.

## 2. EXPERIMENTAL AND METHODS

**2.1. Sample Preparation.** The 5 wt % Pt/Al<sub>2</sub>O<sub>3</sub> catalyst was prepared by the Catalyst Division of Chimet S.p.A. following a deposition–precipitation proprietary protocol similar to that reported by Kaprielova et al.<sup>35</sup> using a high surface area transition alumina (SSA = 116 m<sup>2</sup>g<sup>−1</sup>; pore volume = 0.41 cm<sup>3</sup>g<sup>−1</sup>) as the support. After the Pt deposition, the sample was water-washed and then dried at 120 °C overnight. The same sample was the object of an extensive experimental investigation in the past years as reported in ref 26. The catalyst is characterized by a high metal dispersion ( $D = 63\%$ ) as determined by means of the H<sub>2</sub>/O<sub>2</sub> titration method<sup>15</sup> and confirmed by both TEM and XAS.<sup>26</sup> The analysis of TEM pictures over more than 700 particles indicated a narrow size distribution corresponding to 1.4 ± 0.4 nm.

## 2.2. Inelastic Neutron Scattering (INS) Spectroscopy.

Two INS experiments were performed on the Pt/Al<sub>2</sub>O<sub>3</sub> catalyst under different  $P(\text{H}_2)_{\text{eq}}$  and temperature conditions.<sup>36,37</sup> In the following, the two experiments will be labeled as (1) and (2). Prior to both the INS measurements, the sample was degassed in dynamic vacuum up to 10<sup>-3</sup> mbar in order to remove physisorbed water, then reduced in H<sub>2</sub> atmosphere, and finally further outgassed in order to remove the water and the residual H atoms adsorbed on the Pt clusters which may have been generated during the reduction step. The effective removal of these residual Pt–H species was verified by comparing the INS spectrum of the reduced Pt/Al<sub>2</sub>O<sub>3</sub> catalyst with that of the bare Al<sub>2</sub>O<sub>3</sub> support after degassing at 393 K, as shown in Figure S1 in the Supporting Information. The two INS spectra are almost identical, indicating that there are no residual Pt–H species or, if present, they are below the spectral sensitivity. The sample activation preceding the INS measurements in the two experiments presented some differences, as schematically shown in Figure 1a: for experiment (1), both the outgassing and reduction steps were performed at a temperature of 393 K. For experiment (2), instead, the outgassing steps were performed at 573 K and the reduction in H<sub>2</sub> at 393 K. In both cases, the sample outgassing steps were performed at a significantly higher temperature than the measurement temperature, in order to avoid any further removal of the hydroxyl group at the surface of the alumina during the measurement which, in turn, would result in changes in the spectral features. All the subsequent sample handling was performed inside a glovebox in order to prevent any contamination with moisture and catalyst reoxidation.

Both experiments were performed on the IN1-Lagrange instrument<sup>38</sup> at the ILL in Grenoble, France, which allows measuring energy transfer values up to 4000 cm<sup>-1</sup> (500 meV) with an energy resolution of  $\Delta E/E = 2\%$ . All the spectra were collected in the 90–2900 cm<sup>-1</sup> range of energy transfer by using the Si311 and Cu220 monochromators. For both the experiments, the sample was inserted into an aluminum cell mounted on a gas injection stick and connected to a gas injection device with calibrated volumes.

The two experiments were designed to investigate the sample under different H-coverage conditions, higher for experiment (1) than for experiment (2). Figure 1B locates the two experiments in the  $P(\text{H}_2)_{\text{eq}}-T$  thermodynamic diagram, which displays the expected most stable morphologies and H-coverages for the case of Pt<sub>13</sub>H<sub>y</sub>/γ-Al<sub>2</sub>O<sub>3</sub>(100) system as calculated in ref 19. The two chosen points in the diagram correspond to very different DFT-predicted H-coverage levels (Pt<sub>13</sub>H<sub>34</sub> for experiment (1) and Pt<sub>13</sub>H<sub>6–18</sub> for (2)) but also different morphologies (cuboctahedric geometry for experiment (1), and biplanar for (2)).<sup>19</sup> It has to be noted that some differences in the thermodynamic plot are expected when passing from the Pt<sub>13</sub>H<sub>y</sub> clusters to larger Pt<sub>x</sub>H<sub>y</sub> nanoparticles: for instance, analogous simulations on Pt–H species over extended Pt(111) and Pt(100) surface (representative of large Pt particles) pointed out an easier removal of Pt–H species in comparison with Pt<sub>13</sub>H<sub>y</sub>.<sup>19</sup> Considering this and the fact that our catalyst exhibits a particle size distribution of 1.4 ± 0.4 nm, our analysis included models with larger sizes than Pt<sub>13</sub>, as explained in section 2.3.

Experiment (1) consisted in measuring the sample under vacuum and at room temperature in the presence of a 160 mbar equilibrium pressure of H<sub>2</sub>, which was reached with incremental H<sub>2</sub> doses. The measurements were performed at

25 K with the use of a CCR (closed cycle refrigerator) cryostat. Experiment (2) posed some additional challenges, since lower  $P(\text{H}_2)_{\text{eq}}$  and higher temperatures were required to be able to access a significantly lower level of H coverage than in experiment (1). In fact, keeping the same temperature as in experiment (1) and simply decreasing  $P(\text{H}_2)_{\text{eq}}$  would not have been as effective in decreasing the H-coverage, as shown in Figure 1B. Hence, for this experiment the sample was measured under vacuum and in the presence of a smaller amount of H<sub>2</sub> at a temperature of 450 K. The dosed H<sub>2</sub> was almost completely adsorbed by the sample, making the residual equilibrium pressure not detectable by our equipment. However, the amount of H<sub>2</sub> was calculated by applying the perfect gas law, being all the volumes known, and corresponds to a H:Pt ratio of 0.76. Both the gas dosing and the measurement were conducted at the same temperature of 450 K without removing the sample stick from the instrument. This was possible thanks to a new heating insert setup inside the CCR cryostat now available on the IN1-Lagrange instrument. Previous test measurements on this same sample demonstrated that measuring the INS spectra at temperature higher than 25 K (up to 573 K) does not cause a deterioration of the signal but only a change in the background profile at low energy transfer values that is due to the variation in the population of the vibrational energy levels. To compare the spectra measured during experiment (2) with those measured at cryogenic temperature during experiment (1), the former were corrected by the corresponding Bose–Einstein factor. Further details on this procedure and the original uncorrected spectra are reported in the Supporting Information, section S2.

**2.3. Computational Details.** The experimental INS spectra were interpreted on the basis of DFT simulations on Pt<sub>x</sub>H<sub>y</sub>/γ-Al<sub>2</sub>O<sub>3</sub> model systems. All the structural and vibrational simulations were performed with the VASP package,<sup>39,40</sup> by employing the PBE functional<sup>41</sup> and the projector augmented wave (PAW) pseudopotentials,<sup>42</sup> with a cutoff energy of 400 eV and a convergence criterion for SCF cycles of 10<sup>-6</sup> eV. The models consist in slabs of a dehydroxylated γ-Al<sub>2</sub>O<sub>3</sub>(100) surface or of partially hydroxylated γ-Al<sub>2</sub>O<sub>3</sub>(110) surface (following refs 43–46), upon which Pt<sub>x</sub>H<sub>y</sub> nanoparticles at various H-coverages and for various sizes (x = 13, 34, 38, 55) were supported. The sizes chosen for these Pt clusters correspond to the range of sizes measured by TEM (1.4 ± 0.4 nm),<sup>26</sup> as shown in Table S2 in the Supporting Information. Hereafter, we will use the shorted notation Pt<sub>x</sub>H<sub>y</sub>/γ-Al<sub>2</sub>O<sub>3</sub>(100) and Pt<sub>x</sub>H<sub>y</sub>/γ-Al<sub>2</sub>O<sub>3</sub>(110) to refer to models supported on the two different γ-Al<sub>2</sub>O<sub>3</sub> surfaces, without indicating explicitly the hydroxylation degree anymore. Some complementary calculations have also been run on hydrogenated Pt(111) and Pt(100) surfaces considering previous analysis reported in<sup>19</sup> and described in more detail in section S7 in the Supporting Information.

The most stable structures of the Pt<sub>13</sub>H<sub>y</sub> models at various H-coverages on the two γ-Al<sub>2</sub>O<sub>3</sub> surfaces were previously obtained by means of velocity scale molecular dynamics calculations followed by a quenching procedure as described in refs 19,20, while the larger models were obtained in the present work by static optimization because of computational cost. Further computational details over the simulated models are reported in section S3 of the Supporting Information. Overall, 26 INS spectra of Pt<sub>x</sub>H<sub>y</sub>/γ-Al<sub>2</sub>O<sub>3</sub>(100) and Pt<sub>x</sub>H<sub>y</sub>/γ-Al<sub>2</sub>O<sub>3</sub>(110) models were computed. For all the systems, the geometry optimization and frequency calculations (finite

differences, elongation  $\pm 0.01$  Å) were performed, and finally the obtained outputs were elaborated with the software aCLIMAX<sup>47</sup> to simulate the corresponding INS spectra. Considering the relatively low amount of Pt–H species in the sample and on the basis of our previous experience,<sup>48</sup> we only included the  $0 \rightarrow 1$  transition in the calculated INS spectra. For the analysis of the data in experiment (1) we also performed a linear combination fit analysis: more details about this procedure are described in the Supporting Information, section S4.

### 3. RESULTS AND DISCUSSION

**3.1. Experimental INS Spectra.** The INS spectra of the bare Pt/Al<sub>2</sub>O<sub>3</sub> catalyst activated following procedures (1) and (2) are compared in Figure 2A. They are dominated by the

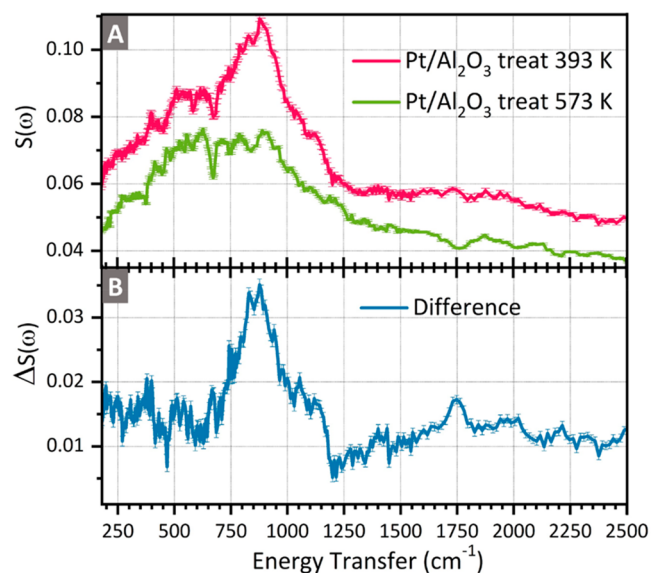


**Figure 2.** Experimental INS spectra of the Pt/Al<sub>2</sub>O<sub>3</sub> catalyst activated following procedures (1) and (2) (A) and their difference, highlighting the spectral profile of the –OH groups at the alumina support which are removed in the 393–573 K activation temperature range (B).

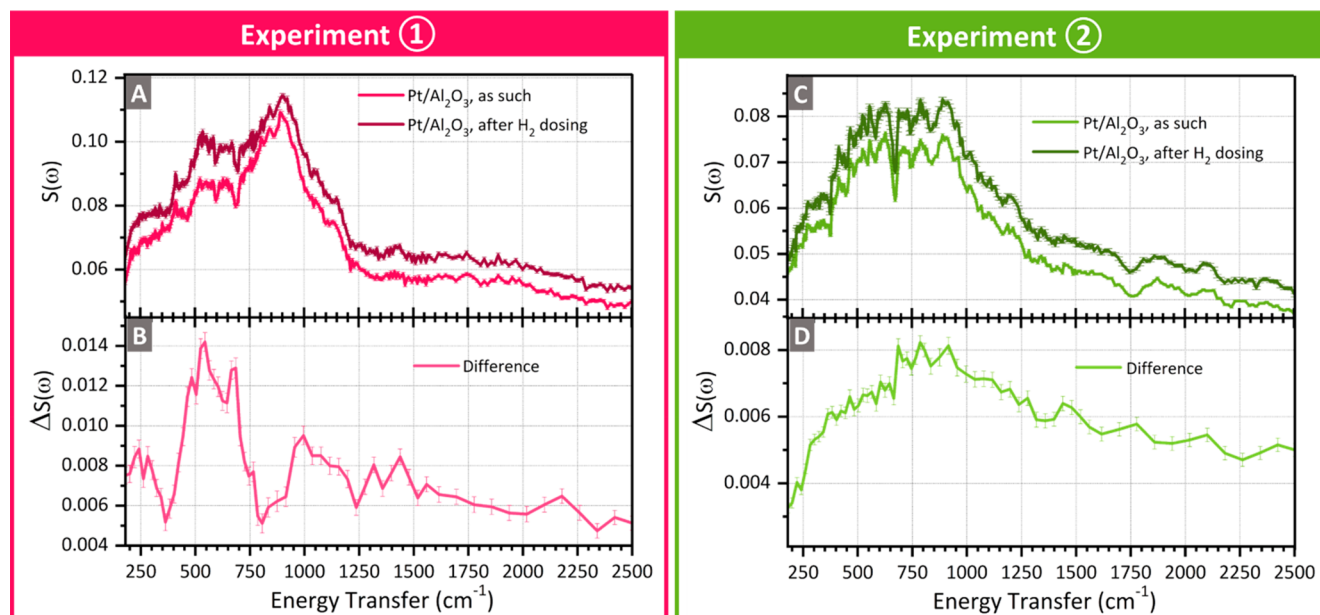
signals relative to the H-containing species in the sample, which are assigned exclusively to the –OH groups at the alumina surface (since no residual Pt–H signals are expected, as justified in section 2.2). More precisely, the very broad band ranging between 200 and 1200 cm<sup>–1</sup> is attributed in the literature to various bending and deformation modes of the –OH groups at the Al<sub>2</sub>O<sub>3</sub> surface.<sup>49</sup> According to the theoretical calculations performed in this work on the  $\gamma$ -Al<sub>2</sub>O<sub>3</sub>(110) supported models, also the riding modes of Al<sub>2</sub>O<sub>3</sub> (i.e., vibrational modes of the Al<sub>2</sub>O<sub>3</sub> surface enhanced in intensity by the presence of the bonded –OH groups) contribute to this spectral range. All those vibrational modes combine to a large extent, with the Al<sub>2</sub>O<sub>3</sub> riding modes contributing mainly to low energy transfer values and the deformation and bending modes of the surface –OH groups to higher ones, but without a clear delimitation between them. Since the –OH groups are progressively removed as the treatment temperature increases,<sup>45,46,50</sup> the difference between the two spectra (Figure 2B) is straightforwardly assigned to the surface hydroxyl groups loss between the temperature of 393 and 573 K during the sample activation.

Figure 3A,C compare the INS spectra of the Pt/Al<sub>2</sub>O<sub>3</sub> samples in vacuum and in the presence of H<sub>2</sub> following the protocols described for experiment (1) and (2), respectively. Following H<sub>2</sub> introduction, the spectra are still dominated by the characteristic features of the hydroxyl species at the Al<sub>2</sub>O<sub>3</sub> surface, but the difference spectra (Figure 3B,D) pointed out the appearance of new bands which are attributed to the formation of new hydrogenous species, including Pt–H species at the surface of the Pt nanoparticles.<sup>26</sup> The intensity of the difference spectrum is greater for experiment (1) than for experiment (2), as expected since the higher  $P(\text{H}_2)_{\text{eq}}$  and the lower temperature favored the formation of a larger amount of Pt–H species. The difference spectra obtained in the two cases also exhibit clearly different spectral profiles, characterized in experiment (1) by a main band centered at about 550 cm<sup>–1</sup> and other weaker bands in the 800–1550 cm<sup>–1</sup> range, and in experiment (2) by a much broader signal centered at about 750 cm<sup>–1</sup>.

**3.2. Theoretical INS Spectra.** In order to precisely assign the experimentally observed Pt–H vibrations, we systematically simulated the INS spectra of 26 different Pt<sub>x</sub>H<sub>y</sub>/ $\gamma$ -Al<sub>2</sub>O<sub>3</sub> models. To ease their interpretation, the spectral contributions of top, 2-fold bridge, 3-fold hollow, and interfacial Pt–H species were separated. Representative examples of each typology of Pt–H species are illustrated in Figure 4A (also displaying their typical Pt–H distances). On this basis, it was possible to assign the vibrational modes involving each class of Pt–H species to specific frequency ranges and to analyze the spectral differences among the models, as summarized in Figure 4B.

The contributions between 250 and 800 cm<sup>–1</sup> correspond to the bending modes of all the Pt–H species vibrating together. These modes are strongly coupled, and only for the highest symmetry models (Pt<sub>13</sub>H<sub>32–36</sub> or Pt<sub>53</sub>H<sub>91</sub>) is it possible to partially distinguish between the bending modes of top Pt–H species (spanning over the 500–580 cm<sup>–1</sup> range) and of bridge species (covering the 530–710 cm<sup>–1</sup> interval). The energy transfer range 800–1600 cm<sup>–1</sup> is dominated by the stretching modes of the multifolded Pt–H species. The  $\nu(\text{Pt–H})$  of 3-fold hollow species is observed in the 850–1300 cm<sup>–1</sup> range, while the asymmetric and symmetric stretching modes of 2-fold bridged species fall in the 800–1200 cm<sup>–1</sup> and 1200–1600 cm<sup>–1</sup> ranges, respectively. Finally, the  $\nu(\text{Pt–H})$  mode of top species contributes within the 2050–2380 cm<sup>–1</sup> range.

For bridge Pt–H species, larger asymmetry in bond lengths corresponds to  $\nu(\text{Pt–H})$  modes spread over a larger interval of frequencies. In most cases, very asymmetric Pt–H bond lengths were observed when the Pt atom is directly bonded to the support. These Pt–H species exhibit Pt–H–Pt bond lengths which pose them in an intermediate position between pure bridge and top species and, for this reason, they were labeled as top-bridge species (see Figure 4A, right as an example). These species exhibit stretching modes within the 1600–1800 cm<sup>–1</sup> interval, the more asymmetric the bond, the higher the stretching frequency. Top sites facing the support can also exhibit a peculiar elongation of the Pt–H bond, often above 1.60 Å instead of the usual 1.57–1.58 Å value (Figure 4A, central), which corresponds to a shift of the stretching mode at a frequency lower than 2000 cm<sup>–1</sup>. These interfacial Pt–H species are favored in close proximity to low-coordinated pentahedral Al<sup>3+</sup> sites at the support surface, with H–Al distances of about 2 Å. For both interfacial top and top-bridge Pt–H species, the effect of the support is stronger



**Figure 3.** (A) experimental INS spectra of Pt/Al<sub>2</sub>O<sub>3</sub> activated according to procedure (1) and of the same sample after dosing H<sub>2</sub> up to a  $P(\text{H}_2)_{\text{eq}} = 160$  mbar at room temperature. (B) Difference between the two spectra shown in panel A. (C) Experimental INS spectra of Pt/Al<sub>2</sub>O<sub>3</sub> activated according to procedure (2) and of the same sample after dosing a low amount of H<sub>2</sub> (resulting in a negligible residual pressure and to a H:Pt ratio of 0.76) at a temperature of 450 K. Both the spectra have been corrected for the temperature effect. (D) Difference between the two spectra shown in panel C. In panels B and D, the subtraction was performed over 5-points rebinned spectra in order to reduce the error bars.

when the Pt nanoparticles are placed on the completely dehydroxylated  $\gamma$ -Al<sub>2</sub>O<sub>3</sub>(100) surface than on the partially hydroxylated  $\gamma$ -Al<sub>2</sub>O<sub>3</sub>(110). More detailed examples of the spectral features of top-bridge and interfacial top Pt–H species, together with the values for the Pt–H and H–Al distances involved, are shown in section S5 in the Supporting Information.

A selection of the simulated INS spectra is shown in Figure 5, while the others are shown in the Supporting Information, section S6. The effects of increasing the Pt nanoparticles' size (from left to right) and of the H-coverage (from top to bottom) are highlighted. In all the cases, the simulated spectra have been also decomposed into the contributions of top, 2-fold bridge, and 3-fold hollow Pt–H species. All the vibrational modes are highly collective, meaning that each of them simultaneously involves several Pt–H species over the whole nanoparticle. This makes the final simulated spectra a unique fingerprint depending on the model shape, size, total H-coverage and typology of Pt–H species formed at the surface of the Pt nanoparticles. In addition, the absolute intensity of the INS spectra is able to provide information about the amount of H present in the model, as the integrated area of the spectra linearly scales with the H-content (analogously to what was pointed out in the past on other classes of samples).<sup>51</sup>

The effect of increasing the H-coverage and of the consequent morphological reconstruction<sup>19</sup> on the INS spectra of Pt<sub>13</sub>H<sub>*y*</sub>/γ-Al<sub>2</sub>O<sub>3</sub>(100) models can be observed in Figure 5A–C. The first model (Figure 5A) consists in a biplanar structure in strong interaction with the support and featuring a comparable number of bridge and top Pt–H species. Its INS spectrum is dominated by a very broad group of bands corresponding to the  $\delta(\text{Pt–H})$  modes, with a maximum at about 400 cm<sup>−1</sup>. As a consequence of the irregular shape of the model and of the variable lengths of the Pt–H bonds, the frequencies of the  $\nu(\text{Pt–H})$  are very spread over a large

interval of frequencies. The effect of the support on the interfacial Pt–H species is highlighted by the presence of bands in the 1800–2000 cm<sup>−1</sup> range, as commented above. The simulated spectrum drastically changes when the reconstruction to a cuboctahedral structure is initiated (Pt<sub>13</sub>H<sub>20</sub> in Figure 5B), both as a consequence of the morphological modification and of the conversion of top Pt–H species into bridge ones, resulting in bands spanning over much narrower frequency intervals (500–800 cm<sup>−1</sup> for the  $\delta(\text{Pt–H})$  modes and 800–1600 cm<sup>−1</sup> for the  $\nu(\text{Pt–H})$  ones). Similar features are retained for the completely reconstructed model in cuboctahedral geometry (Figure 5C), where the main changes arise from the formation of new top Pt–H species upon the complete H-solvation of the nanoparticle (contributing in the 2000–2250 cm<sup>−1</sup> range). Analogous trends were observed for the Pt<sub>13</sub>H<sub>*y*</sub>/γ-Al<sub>2</sub>O<sub>3</sub>(110) models (Figure S8 in the Supporting Information), with the most significant spectral differences arising from the lack of top-bridge and interfacial top Pt–H features.

By moving from left to right in Figure 5, it is instead possible to evaluate the effect of the change in shape and size of the hydrogenated Pt nanoparticle on the INS spectra. Model Pt<sub>34</sub>H<sub>54</sub> (Figure 5D) features a quite irregular geometry, resulting in a spectrum where the  $\delta(\text{Pt–H})$  and the  $\nu(\text{Pt–H})$  bands of both bridge and top species span over a large frequency interval. Only one and very asymmetrical hollow Pt–H site is present. From Pt<sub>38</sub>H<sub>72</sub> onward, the considered models are large enough to expose well-recognizable facets. Indeed, model Pt<sub>38</sub>H<sub>72</sub> (Figure 5E) corresponds to a truncated octahedron structure exposing quite large hexagonal Pt(111) facets and smaller squared Pt(100) ones, while the Pt<sub>55</sub>H<sub>*y*</sub> models (Figure 5F–H) were optimized starting from a cuboctahedron structure exposing triangular Pt(111) facets and squared Pt(100) ones. The exposed facets are shown more clearly in Figure S7 in the Supporting Information. As bridge

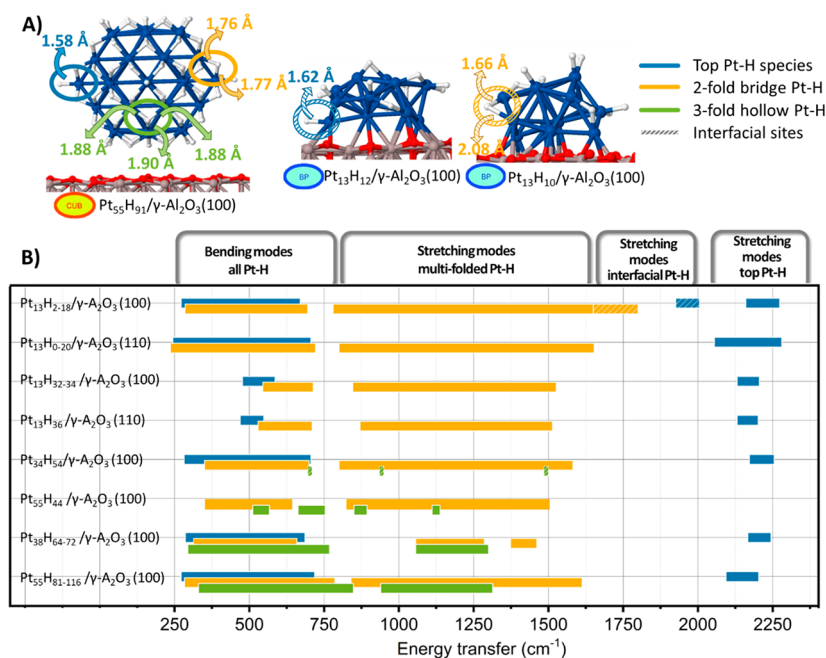


**Figure 4.** (A) Representative geometry of top (blue), 2-fold bridge (yellow), 3-fold hollow (green), and interfacial (lined pattern) Pt–H species. The typical bond lengths for each of these Pt–H species are also reported. (B) Summary of the characteristic position of the INS signals for the different types of Pt–H species in the simulated models. The general assignment into stretching and bending for top, bridge, hollow, and interfacial Pt–H is also indicated.

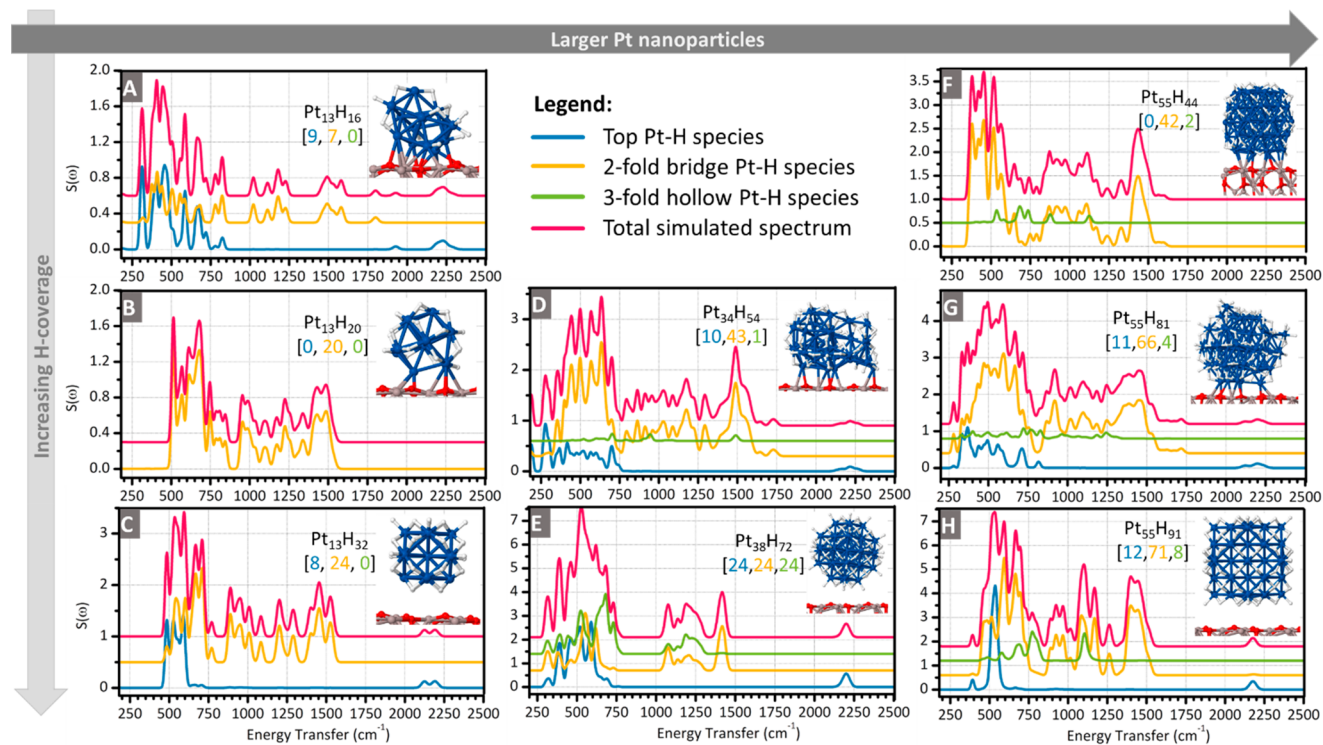


**Figure 5.** Simulated INS spectra for a selection of Pt<sub>x</sub>H<sub>y</sub>/γ-Al<sub>2</sub>O<sub>3</sub>(100) models, featuring different sizes, morphologies, and H-coverages. The shown models correspond to (A) Pt<sub>13</sub>H<sub>16</sub>, (B) Pt<sub>13</sub>H<sub>20</sub>, (C) Pt<sub>13</sub>H<sub>32</sub>, (D) Pt<sub>34</sub>H<sub>54</sub>, (E) Pt<sub>38</sub>H<sub>72</sub>, (F) Pt<sub>55</sub>H<sub>44</sub>, (G) Pt<sub>55</sub>H<sub>81</sub>, (H) Pt<sub>55</sub>H<sub>91</sub>. The spectra are decomposed into the contributions of top (blue), 2-fold bridge (orange) and 3-fold hollow (green) Pt–H species. The geometry of the models corresponding to each spectrum are reported, together with their Pt<sub>x</sub>H<sub>y</sub> stoichiometry and the number of top, bridge, and hollow Pt–H species present in the model in the form [top, bridge, hollow].

species are the most stable on the Pt(100) surface<sup>52</sup> and fcc hollow ones are the most stable on the Pt(111) one,<sup>53</sup> the number of bridge and hollow Pt–H species in the optimized geometries vary greatly depending on the most exposed facets

in the model. Top Pt–H species is preferentially located at the edges and corners between the faces. The simulation of a Pt<sub>55</sub>H<sub>91</sub> model with icosahedral shape was also attempted, but its geometry collapsed onto a distorted cuboctahedron both in

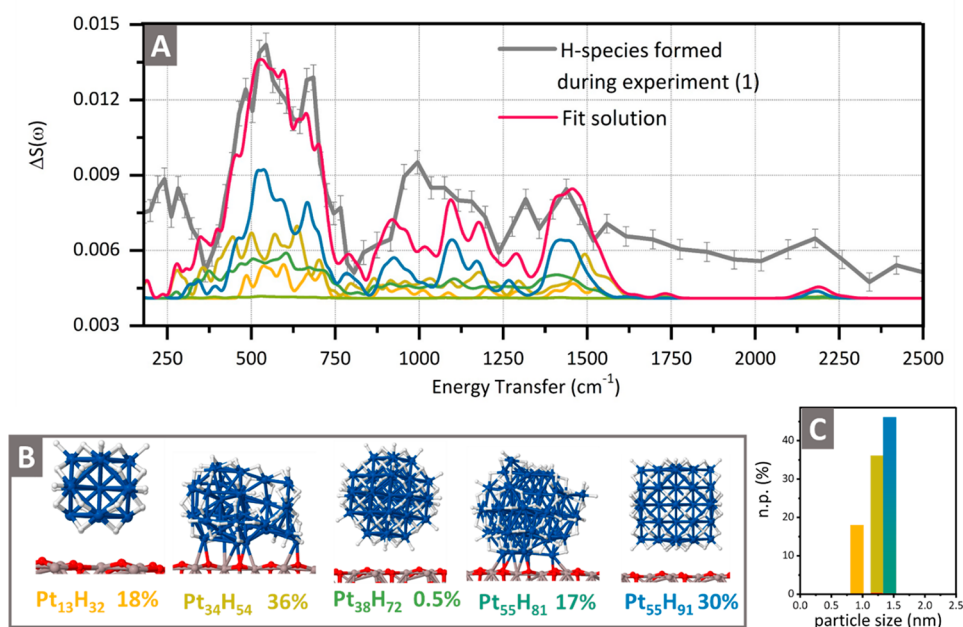


**Figure 6.** (A) Experimental INS difference spectrum containing the fingerprint of the Pt–H species formed at Pt/Al<sub>2</sub>O<sub>3</sub> at high H-coverage compared with the best linear combination fit performed with the simulated spectra of Pt<sub>13</sub>H<sub>32</sub>, Pt<sub>34</sub>H<sub>54</sub>, Pt<sub>38</sub>H<sub>72</sub>, Pt<sub>55</sub>H<sub>81</sub>, and the two Pt<sub>55</sub>H<sub>91</sub> models on the dehydroxylated  $\gamma$ -Al<sub>2</sub>O<sub>3</sub> (100) surface. (B) Models included in the fit and their weight in the final solution. (C) Corresponding simulated Pt nanoparticles size distribution.

the preliminary optimization performed on the isolated nanoparticle and on the one including the support, suggesting that an icosahedral habit does not correspond to an energetic minimum for small hydrogenated Pt nanoparticles. The spectrum of the truncated octahedron Pt<sub>38</sub>H<sub>72</sub> model (Figure 5E) exhibits a large  $\delta$ (Pt–H) band spanning over the 250–750 cm<sup>-1</sup> interval and a relatively narrow spectral region corresponding to the  $\nu$ (Pt–H) of multifolded species between 1000 and 1500 cm<sup>-1</sup>. The Pt<sub>55</sub>H<sub>y</sub> models instead (Figure 5F–H), corresponding to larger cuboctahedral-based geometries, exhibit spectra characterized by a progressive shift of the  $\delta$ (Pt–H) region from lower to higher frequencies as the H-coverage increases, with the  $\nu$ (Pt–H) of multifolded species spanning over the whole 800–1600 cm<sup>-1</sup> interval. In many respects, the two groups of cuboctahedral models Pt<sub>55</sub>H<sub>y</sub> and Pt<sub>13</sub>H<sub>y</sub> show similar spectral profiles, while the truncated octahedra Pt<sub>38</sub>H<sub>y</sub> result readily distinguishable. Also in this case, very symmetric structures can be optimized only at the highest H-coverage levels.

Finally, in addition to those Pt<sub>x</sub>H<sub>y</sub>/ $\gamma$ -Al<sub>2</sub>O<sub>3</sub> models, the INS spectra of bridged Pt–H species at the extended Pt(100) surface and the top and hollow ones at the Pt(111) surface were also simulated. The obtained spectra are shown and commented in the Supporting Information, section S7.

Generalizing the observations summarized above, the simulated INS spectra arise from the combination of multiple factors, among which are the following: (i) the ratio between top, bridge, and hollow Pt–H species; (ii) their relative position; (iii) the shape of the model, (iv) its size, and (v) its interaction with the support, in a way that makes each INS spectrum the fingerprint of the corresponding model. It is important to notice that the proposed assignments are in generally good agreement with those proposed in the past not only for INS spectra<sup>30,31</sup> but also for other vibrational spectra (such as FT-IR<sup>26</sup> or EELS<sup>52</sup>), as well as with other computational simulations.<sup>34</sup> However, most of the assign-

ments in the literature were based on measurements on extended Pt surfaces or simulations on isolated Pt clusters. In this regard, our results provide a picture closer to the real catalyst under H<sub>2</sub> atmosphere, since they also take into account the modifications introduced by the support and the effects of the size, shape, and H-coverage of the Pt nanoparticles.

**3.3. Comparison between Experiments and Simulations.** **3.3.1. Higher H-Coverage Conditions.** On the basis of the information collected from the simulated INS spectra presented in section 3.2, we proceeded with the interpretation of the difference experimental INS spectrum containing the fingerprint of the Pt–H species formed during experiment (1) (Figure 3B). None of the models is able to completely describe the experimental spectrum alone: indeed, Pt/Al<sub>2</sub>O<sub>3</sub> is characterized by a more heterogeneous nature than any of the considered models in terms of nanoparticles size, shape, and interaction with the support. For this reason, a linear combination fit analysis of the experimental spectrum with the simulated ones was performed. In order to ensure the robustness of the fit calculation, we had to limit the number of simulated functions to be included, which were selected on the basis of the best agreement with the experimental spectrum to be fitted. Following the procedure explained in more detail in section S4 in the Supporting Information, five models were included: Pt<sub>13</sub>H<sub>32</sub>, Pt<sub>34</sub>H<sub>54</sub>, Pt<sub>38</sub>H<sub>72</sub>, Pt<sub>55</sub>H<sub>81</sub> and Pt<sub>55</sub>H<sub>91</sub>, which are in good agreement with the observed TEM sizes (as explained in section S3 in the Supporting Information). According to the linear combination fit analysis reported in Figure 6, the following interpretations can be proposed:

- (1) The main model contributing to the fit is the irregular model Pt<sub>34</sub>H<sub>54</sub> (accounting for 36%), followed by the cuboctahedral based models Pt<sub>55</sub>H<sub>91</sub> and Pt<sub>55</sub>H<sub>81</sub> (30% and 17%) and then by the smaller cuboctahedron Pt<sub>13</sub>H<sub>32</sub> (18%).

- (2) All the models included into the fit are characterized by a H:Pt ratio larger than 1. However, the model with the highest H-coverage ( $\text{Pt}_{55}\text{H}_{116}$ , see Supporting Information, Figure S6D) is characterized by remarkably different spectral features, suggesting that the H-coverage reached during this experiment was not the highest possible.
- (3) In all the included models, the Pt nanoparticle shows a weak interaction with the support, in particular the cuboctahedral  $\text{Pt}_{13}\text{H}_{32}$  and  $\text{Pt}_{55}\text{H}_{91}$  models. The fit highlights that both regular geometries (such as  $\text{Pt}_{13}\text{H}_{32}$  and  $\text{Pt}_{55}\text{H}_{91}$ ) and less regular ones (such as  $\text{Pt}_{55}\text{H}_{81}$  and, even more so,  $\text{Pt}_{34}\text{H}_{54}$ ) are needed to describe the experimental spectrum. Among the regular shapes, cuboctahedra such as  $\text{Pt}_{13}\text{H}_y$  and  $\text{Pt}_{55}\text{H}_y$  models are favored over the  $\text{Pt}_{38}\text{H}_y$  truncated octahedron, whose occurrence according to the fit is lower than 1%.
- (4) It was not possible to discriminate between nanoparticles supported on the two considered  $\gamma\text{-Al}_2\text{O}_3$  surfaces (dehydroxylated (100) one or partially hydroxylated (110)) as the spectral features corresponding to the two sets of models were extremely similar, in particular for nanoparticles in very weak interaction with the support (compare Figure 5A–C with Figure S8 in the Supporting Information).

Quite remarkably, the particle size distribution suggested by the linear combination fit analysis (Figure 6C) is in very good accordance with that determined experimentally by means of TEM and confirmed by XAS.<sup>26</sup>

Although the best linear combination fit reproduces most of the experimental bands, some spectral regions (in particular around 250, 1000, and 1300  $\text{cm}^{-1}$ ) are not well described. Since the spectral features are strongly related to the shape and size of the nanoparticle, the main possible source for this residual discrepancy could be attributed to the lack of diversity in the considered nanoparticle morphology, size, and/or H-coverage in our simulations set. One possibility is given by Pt–H species formed over more extended Pt(100) and Pt(111) surfaces, which could be exposed by the largest nanoparticles in the sample (although rare, nanoparticles as large as 2.5–3.0 nm were detected by TEM<sup>26</sup>). For exploring this possibility, the INS spectra of bridged Pt–H species on the Pt(100) extended surface, and top and hollow Pt–H at the Pt(111) one were also considered (Supporting Information, section S7). On the basis of those simulations, the missing signal at 250  $\text{cm}^{-1}$  may be attributed to top Pt–H species at extended Pt(111) surfaces, while hollow Pt–H species at Pt(111) surfaces might be responsible of the signal at 1000  $\text{cm}^{-1}$ . The possible attribution to other H containing species instead, such as new –OH species formed at the support, is presently considered improbable because the spectral ranges do not match, as shown in Figure S11 in the Supporting Information.

**3.3.2. Lower H-Coverage Conditions.** In the case of the INS spectra measured during experiment (2), the amount of new hydrogenous species formed upon dosing  $\text{H}_2$  was significantly lower than in experiment (1), resulting in a difference signal which was too weak and broad to perform a quantitative evaluation. However, a qualitative assignment was still possible by comparing the available experimental and simulated data, as summarized in Figure 7. First of all, the most intense signal at about 800  $\text{cm}^{-1}$  exhibits a remarkable similarity to that reported in Figure 2B and ascribed to surface

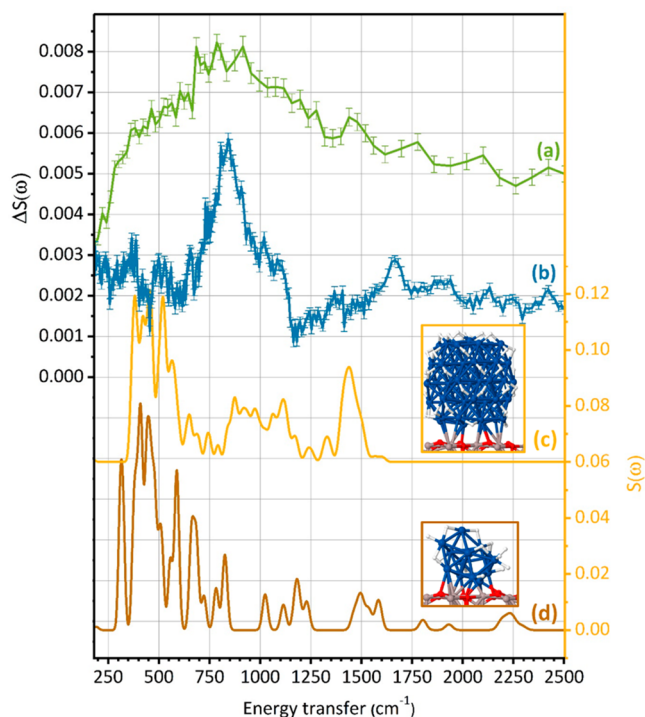


**Figure 7.** Comparison among: (a) the differential INS spectrum containing the spectral fingerprint of the species formed on  $\text{Pt}/\text{Al}_2\text{O}_3$  during experiment (2) (same as in Figure 3D); (b) differential INS spectrum ascribed to surface –OH species removed in the temperature range 393–573 K (same as in Figure 2B, scaled by a factor 6 for a better comparison); (c) simulated spectrum of the low-coverage  $\text{Pt}_{55}\text{H}_{44}/\gamma\text{-Al}_2\text{O}_3(100)$  model, and (d) simulated spectrum of  $\text{Pt}_{13}\text{H}_{16}/\gamma\text{-Al}_2\text{O}_3(100)$ . The geometries of the two models are shown for clarity, and the intensities of the simulated spectra were normalized to the number of H atoms in the respective models.

–OH groups. This suggests that at a significant part of the new H-containing species formed during this experiment are due to the formation of new surface –OH groups, as a result of H-spillover.<sup>54,55</sup> The presence of this signal in the difference spectra of experiment (2), and not of experiment (1), could be a consequence of the different activation procedures followed in the two experiments (Figure 1A). Indeed, in the present experiment, the sample was activated at a significantly higher temperature (573 vs 393 K), and thus a larger fraction of surface –OH groups was lost during activation. According to previous DFT calculations,<sup>45,46,56,57</sup> the  $\gamma\text{-Al}_2\text{O}_3(110)$  lateral surface is the most sensitive to –OH group loss within this interval of treatment temperature, while the (100) is almost completely dehydroxylated in this range. Furthermore, previous reports concluded that exposed low-coordinated  $\text{Al}^{3+}$  sites are necessary for the occurrence of H-spillover<sup>54</sup> and that this typology of highly reactive sites exists on the  $\gamma\text{-Al}_2\text{O}_3(110)$  surface and stabilizes H-species upon high temperature treatment.<sup>56,58</sup> More generally, such defective sites may also exist on the edges of alumina platelets as recently shown.<sup>59</sup> On these premises, we hypothesize that the H-spillover process observed in our experiment is related to the formation of new –OH groups at the  $\text{Al}_2\text{O}_3(110)$  surface. However, we cannot exclude that the observed difference arose because of kinetics reasons. In fact,  $\text{H}_2$  was dosed at a significantly higher temperature in experiment (2) than in (1) (450 vs 300 K). Furthermore, in (2) the whole measurement

was performed at that same temperature, while in (1) the sample was quenched at 25 K prior to the measurement. Thus, H-spillover could have been kinetically favored during experiment (2) and not during (1).

The signal at lower energy transfer (centered at about 450  $\text{cm}^{-1}$ ), instead, falls in the range typical for  $\delta(\text{Pt}-\text{H})$  modes, in particular for models characterized by a H:Pt ratio close to 1 or lower and exhibiting a strong interaction with the  $\gamma\text{-Al}_2\text{O}_3$  support. As an example, the structures and the simulated spectra for  $\text{Pt}_{55}\text{H}_{44}$  and  $\text{Pt}_{13}\text{H}_{16}$  are shown in Figure 7c,d. The broad tail in the experimental INS spectrum at energy transfer values higher than 950  $\text{cm}^{-1}$  is also compatible with the signals of  $\nu(\text{Pt}-\text{H})$  of bridge and hollow Pt–H species. In particular, the signal at about 1475  $\text{cm}^{-1}$  strongly resembles the profile of both the simulated spectra shown in Figure 7.

Overall, these qualitative observations are in accordance with the thermodynamic calculations on  $\text{Pt}_{13}\text{H}_y$  clusters<sup>19,20</sup> that, at the temperature and  $P(\text{H}_2)_{\text{eq}}$  conditions here adopted, predicted a H coverage in the range  $\text{Pt}_{13}\text{H}_{6-18}$ , confirming that it is possible to distinguish between low and high H-coverage in supported  $\text{Pt}_x\text{H}_y$  nanoparticles from their INS spectra.

#### 4. CONCLUSIONS

The reactive adsorption of  $\text{H}_2$  with Pt nanoparticles on transition alumina is predicted to trigger significant changes in the nanoparticles morphology and in their interaction with the support as a function of temperature and  $P(\text{H}_2)_{\text{eq}}$ .<sup>19,20</sup> Although a few experimental studies by XAS and IR spectroscopy confirm the theoretical predictions, direct experimental evidence on all the types of surface Pt–H species and on their interconversion during Pt nanoparticles reconstruction are still limited. Herein, we addressed this challenge by analyzing the behavior of an industrial highly dispersed 5 wt %  $\text{Pt}/\text{Al}_2\text{O}_3$  catalyst characterized by a narrow particle size distribution under hydrogenation conditions by means of INS spectroscopy combined with DFT simulations.

Two experiments were conducted under different  $\text{H}_2$  pressure and T conditions, corresponding to higher H-coverages for experiment (1) than for experiment (2). Albeit the weak intensity of the difference INS spectra, the high sensitivity of modern spectrometers allowed us to obtain the INS fingerprints of the hydrogenous species generated under these two conditions. The two experimental spectra were interpreted on the basis of DFT and INS spectra simulations on 26  $\text{Pt}_x\text{H}_y/\gamma\text{-Al}_2\text{O}_3$  models.<sup>19,20</sup> Remarkable variations were observed as a function particle sizes ( $x$ ), H-coverages ( $y/x$ ), and morphologies, revealing that INS spectroscopy is able to provide a fine description of the  $\text{Pt}/\text{Al}_2\text{O}_3$  system under different hydrogenation conditions. Two relevant  $\gamma\text{-Al}_2\text{O}_3$  surfaces at different hydroxylation states were also considered: the completely dehydroxylated (100) surface and the partially hydroxylated (110) one (following refs 43,45,46). It was found that the type of support surface does not affect significantly the simulated INS spectra of the Pt–H species.

For experiment (1), the INS spectrum was satisfactorily fitted with a linear combination of a few simulated spectra corresponding to Pt nanoparticles characterized by a H:Pt ratio much larger than 1 and by a weak interaction with the alumina support. The analysis also pointed out that the best solution favors a particle size in the  $\text{Pt}_{34}\text{H}_y\text{-Pt}_{55}\text{H}_y$  range, in good agreement with that determined by TEM and confirmed by XAS.<sup>26</sup> In addition, it allowed us to conclude the coexistence of

both irregular morphologies, such as  $\text{Pt}_{34}\text{H}_{54}$ , and very symmetric ones, such as  $\text{Pt}_{55}\text{H}_{91}$ . Also among the regular morphologies, cuboctahedra are strongly favored over truncated octahedra shapes. Some complementary contributions are suspected to originate from Pt–H species located on more extended Pt(111) surface present on a few larger Pt nanoparticles. Furthermore, it has to be noticed how the weakening of the interaction with the support upon complete solvation might also increase the probability for nanoparticles sintering, with possible consequences concerning the catalyst longevity and deactivation.

As for experiment (2) instead, the spectral interpretation was more challenging because of the very weak intensity and broadness of the difference spectrum. We were however able to proceed with a qualitative assignment: the spectral features of the newly formed hydrogenous species are compatible with the formation of new hydroxyls at the support surface, likely as a consequence of H-spillover from the metal nanoparticles to the support, and with the characteristic spectral features of  $\text{Pt}_x\text{H}_y$  nanoparticles with a H:Pt ratio close or lower than 1 and in strong interaction with the support, such as for the  $\text{Pt}_{55}\text{H}_{44}$  or the  $\text{Pt}_{13}\text{H}_{16}$  models.

Overall, our data confirm that Pt nanoparticles undergo important changes in terms of morphology, degree of interaction with the support and types of Pt–H species (top, bridge, hollow) formed as a function of the hydrogenation conditions (temperature and  $P(\text{H}_2)_{\text{eq}}$ ), providing unprecedented vibrational spectra describing the variety of Pt–H species involved in the hydrogenation reactions. The present study is consistent with previously reported theoretical and experimental data, being at the same time able to make a further step in the description of the complexity and heterogeneity of real  $\text{Pt}/\text{Al}_2\text{O}_3$  systems. While previous studies were mostly obtained from simulations and/or experiments performed on Pt surfaces or on isolated cluster systems, the present one is the first systematic investigation quantifying the effect of the particle size, morphology, and H-coverage by INS. It also shows a direct evidence of the occurrence of H-spillover, when the catalyst in preactivated at sufficiently high temperature to significantly reduce the density of –OH groups at the  $\text{Al}_2\text{O}_3$  surface. Finally, we demonstrated the capability of INS spectroscopy, coupled with DFT simulation, to discriminate among  $\text{Pt}_x\text{H}_y$  nanoparticles stabilized under different experimental conditions.

As we underlined in the Introduction,  $\text{Pt}/\text{Al}_2\text{O}_3$  are key catalysts widely used in numerous catalytic processes where dihydrogen is a crucial coreactant used during the activation process or during reaction. In all cases,  $\text{H}_2$  partial pressure must be optimally tuned to control the process selectivity. Hence, from a catalytic standpoint, the results obtained in the present study translate into significant insights into the behavior of  $\text{Pt}/\text{Al}_2\text{O}_3$  catalysts upon reductive  $\text{H}_2$  atmosphere, the available reactive Pt–H species and their modification upon change in the temperature or the  $P(\text{H}_2)_{\text{eq}}$ . Beyond that, our study also provides a solid starting point to further investigate the ductility of the Pt active phase in the presence of reactants and under reaction conditions.

#### ■ ASSOCIATED CONTENT

##### Supporting Information

The Supporting Information is available free of charge at <https://pubs.acs.org/doi/10.1021/acscatal.2c00606>.

Additional material concerning the experiment INS spectra and their data analysis, the simulated Pt<sub>x</sub>H<sub>y</sub>/γ-Al<sub>2</sub>O<sub>3</sub> models and the corresponding calculated INS spectra (PDF)

## AUTHOR INFORMATION

### Corresponding Author

**Eleonora Vottero** – Department of Chemistry, INSTM and NIS Centre, University of Torino, I-10135 Torino, Italy; Institut Laue-Langevin (ILL), 38042 Grenoble, France; [orcid.org/0000-0002-0183-0669](https://orcid.org/0000-0002-0183-0669); Email: [eleonora.vottero@unito.it](mailto:eleonora.vottero@unito.it)

### Authors

**Michele Carosso** – Department of Chemistry, INSTM and NIS Centre, University of Torino, I-10135 Torino, Italy  
**Alberto Ricchebuono** – Department of Chemistry, INSTM and NIS Centre, University of Torino, I-10135 Torino, Italy  
**Monica Jiménez-Ruiz** – Institut Laue-Langevin (ILL), 38042 Grenoble, France; [orcid.org/0000-0002-9856-807X](https://orcid.org/0000-0002-9856-807X)  
**Riccardo Pellegrini** – Chimet SpA - Catalyst Division, I-52041 Vicomaggio Arezzo, Italy  
**Céline Chizallet** – IFP Energies nouvelles, BP3-69360 Solaize, France; [orcid.org/0000-0001-5140-8397](https://orcid.org/0000-0001-5140-8397)  
**Pascal Raybaud** – IFP Energies nouvelles, BP3-69360 Solaize, France; [orcid.org/0000-0003-4506-5062](https://orcid.org/0000-0003-4506-5062)  
**Elena Groppo** – Department of Chemistry, INSTM and NIS Centre, University of Torino, I-10135 Torino, Italy; [orcid.org/0000-0003-4153-5709](https://orcid.org/0000-0003-4153-5709)  
**Andrea Piovano** – Institut Laue-Langevin (ILL), 38042 Grenoble, France; [orcid.org/0000-0002-5005-6307](https://orcid.org/0000-0002-5005-6307)

Complete contact information is available at: <https://pubs.acs.org/10.1021/acscatal.2c00606>

### Notes

The authors declare no competing financial interest.

## REFERENCES

- (1) Gjervan, T.; Prestvik, R.; Holmen, A. Catalytic Reforming. In *Basic Principles in Applied Catalysis*; Baerns, M., Ed.; Springer Berlin Heidelberg: Berlin, Heidelberg, 2004; pp 125–158.
- (2) le Goff, P.-Y.; Kostka, W.; Ross, J. Catalytic Reforming. In *Springer Handbook of Petroleum Technology*, 2nd ed.; Hsu, C. S.; Robinson, P., Eds.; Springer: New York, 2017; pp 589–616.
- (3) Bartok, M. Heterogeneous Catalytic Enantioselective Hydrogenation of Activated Ketones. *Curr. Org. Chem.* **2006**, *10* (13), 1533–1567.
- (4) Sattler, J. J. H. B.; Ruiz-Martinez, J.; Santillan-Jimenez, E.; Weckhuysen, B. M. Catalytic Dehydrogenation of Light Alkanes on Metals and Metal Oxides. *Chem. Rev.* **2014**, *114* (20), 10613–10653.
- (5) Chen, S.; Chang, X.; Sun, G.; Zhang, T.; Xu, Y.; Wang, Y.; Pei, C.; Gong, J. Propane dehydrogenation: catalyst development, new chemistry, and emerging technologies. *Chem. Soc. Rev.* **2021**, *50* (5), 3315–3354.
- (6) Docherty, S. R.; Rochlitz, L.; Payard, P.-A.; Copéret, C. Heterogeneous alkane dehydrogenation catalysts investigated via a surface organometallic chemistry approach. *Chem. Soc. Rev.* **2021**, *50* (9), 5806–5822.
- (7) Keppeler, M.; Bräuning, G.; Radhakrishnan, S. G.; Liu, X.; Jensen, C.; Roduner, E. Reactivity of diatomics and of ethylene on zeolite-supported 13-atom platinum nanoclusters. *Catal. Sci. Technol.* **2016**, *6* (18), 6814–6823.
- (8) Kahlich, M. J.; Gasteiger, H. A.; Behm, R. J. Kinetics of the Selective CO Oxidation in H<sub>2</sub>-Rich Gas on Pt/Al<sub>2</sub>O<sub>3</sub>. *J. Catal.* **1997**, *171* (1), 93–105.
- (9) Gélín, P.; Primet, M. Complete oxidation of methane at low temperature over noble metal based catalysts: a review. *Appl. Catal., B* **2002**, *39* (1), 1–37.
- (10) Sangnier, A.; Genty, E.; Iachella, M.; Sautet, P.; Raybaud, P.; Matrat, M.; Dujardin, C.; Chizallet, C. Thermokinetic and Spectroscopic Mapping of Carbon Monoxide Adsorption on Highly Dispersed Pt/γ-Al<sub>2</sub>O<sub>3</sub>. *ACS Catal.* **2021**, *11* (21), 13280–13293.
- (11) Ren, X.; Lv, Q.; Liu, L.; Liu, B.; Wang, Y.; Liu, A.; Wu, G. Current progress of Pt and Pt-based electrocatalysts used for fuel cells. *Sustainable Energy Fuels* **2020**, *4* (1), 15–30.
- (12) Heck, R. M.; Farrauto, R. J. Automobile exhaust catalysts. *Appl. Catal. A: Gen.* **2001**, *221* (1), 443–457.
- (13) Gänzler, A. M.; Casapu, M.; Vernoux, P.; Loridant, S.; Cadete Santos Aires, F. J.; Epicier, T.; Betz, B.; Hoyer, R.; Grunwaldt, J.-D. Tuning the Structure of Platinum Particles on Ceria In Situ for Enhancing the Catalytic Performance of Exhaust Gas Catalysts. *Angew. Chem., Int. Ed.* **2017**, *56* (42), 13078–13082.
- (14) Gruber, H. L. Chemisorption studies on supported platinum. *J. Phys. Chem.* **1962**, *66* (1), 48–54.
- (15) Benson, J. E.; Boudart, M. Hydrogen-oxygen titration method for the measurement of supported platinum surface areas. *J. Catal.* **1965**, *4* (6), 704–710.
- (16) Vannice, M. A.; Benson, J. E.; Boudart, M. Determination of surface area by chemisorption: Unsupported platinum. *J. Catal.* **1970**, *16* (3), 348–356.
- (17) Zaera, F. New Challenges in Heterogeneous Catalysis for the 21<sup>st</sup> Century. *Catal. Lett.* **2012**, *142* (5), 501–516.
- (18) Boudart, M.; Aldag, A.; Benson, J. E.; Dougharty, N. A.; Girvin Harkins, C. On the specific activity of platinum catalysts. *J. Catal.* **1966**, *6* (1), 92–99.
- (19) Mager-Maury, C.; Bonnard, G.; Chizallet, C.; Sautet, P.; Raybaud, P. H<sub>2</sub>-Induced Reconstruction of Supported Pt Clusters: Metal-Support Interaction versus Surface Hydride. *ChemCatChem.* **2011**, *3* (1), 200–207.
- (20) Gorczyca, A.; Moizan, V.; Chizallet, C.; Proux, O.; Del Net, W.; Lahera, E.; Hazemann, J.-L.; Raybaud, P.; Joly, Y. Monitoring Morphology and Hydrogen Coverage of Nanometric Pt/γ-Al<sub>2</sub>O<sub>3</sub> Particles by In Situ HERFD-XANES and Quantum Simulations. *Angew. Chem., Int. Ed.* **2014**, *53* (46), 12426–12429.
- (21) Wang, L.-L.; Johnson, D. D. Shear Instabilities in Metallic Nanoparticles: Hydrogen-Stabilized Structure of Pt<sub>37</sub> on Carbon. *J. Am. Chem. Soc.* **2007**, *129* (12), 3658–3664.
- (22) Wei, G.-F.; Liu, Z.-P. Restructuring and Hydrogen Evolution on Pt Nanoparticle. *Chem. Sci.* **2015**, *6* (2), 1485–1490.
- (23) Oudenhuijzen, M. K.; van Bokhoven, J. A.; Miller, J. T.; Ramaker, D. E.; Koningsberger, D. C. Three-Site Model for Hydrogen Adsorption on Supported Platinum Particles: Influence of Support Ioncity and Particle Size on the Hydrogen Coverage. *J. Am. Chem. Soc.* **2005**, *127* (5), 1530–1540.
- (24) Sun, G.; Sautet, P. Metastable Structures in Cluster Catalysis from First-Principles: Structural Ensemble in Reaction Conditions and Metastability Triggered Reactivity. *J. Am. Chem. Soc.* **2018**, *140* (8), 2812–2820.
- (25) Timoshenko, J.; Lu, D.; Lin, Y.; Frenkel, A. I. Supervised Machine-Learning-Based Determination of Three-Dimensional Structure of Metallic Nanoparticles. *J. Phys. Chem. Lett.* **2017**, *8* (20), 5091–5098.
- (26) Carosso, M.; Vottero, E.; Lazzarini, A.; Morandi, S.; Manzoli, M.; Lomachenko, K. A.; Ruiz, M. J.; Pellegrini, R.; Lamberti, C.; Piovano, A.; Groppo, E. Dynamics of Reactive Species and Reactant-Induced Reconstruction of Pt Clusters in Pt/Al<sub>2</sub>O<sub>3</sub> Catalysts. *ACS Catal.* **2019**, *9* (8), 7124–7136.
- (27) Vaarkamp, M.; Miller, J. T.; Modica, F. S.; Koningsberger, D. C. On the Relation between Particle Morphology, Structure of the Metal-Support Interface, and Catalytic Properties of Pt/γ-Al<sub>2</sub>O<sub>3</sub>. *J. Catal.* **1996**, *163* (2), 294–305.
- (28) Cabié, M.; Giorgio, S.; Henry, C. R.; Axet, M. R.; Philippot, K.; Chaudret, B. Direct Observation of the Reversible Changes of the

- Morphology of Pt Nanoparticles under Gas Environment. *J. Phys. Chem. C* **2010**, *114* (5), 2160–2163.
- (29) Yakovina, O. A.; Lisitsyn, A. S. Probing the H<sub>2</sub>-Induced Restructuring of Pt Nanoclusters by H<sub>2</sub>-TPD. *Langmuir* **2016**, *32* (46), 12013–12021.
- (30) Albers, P.; Auer, E.; Ruth, K.; Parker, S. F. Inelastic Neutron Scattering Investigation of the Nature of Surface Sites Occupied by Hydrogen on Highly Dispersed Platinum on Commercial Carbon Black Supports. *J. Catal.* **2000**, *196* (1), 174–179.
- (31) Parker, S. F.; Frost, C. D.; Telling, M.; Albers, P.; Lopez, M.; Seitz, K. Characterisation of the adsorption sites of hydrogen on Pt/C fuel cell catalysts. *Catal. Today* **2006**, *114* (4), 418–421.
- (32) Yamazoe, S.; Yamamoto, A.; Hosokawa, S.; Fukuda, R.; Hara, K.; Nakamura, M.; Kamazawa, K.; Tsukuda, T.; Yoshida, H.; Tanaka, T. Identification of hydrogen species on Pt/Al<sub>2</sub>O<sub>3</sub> by in situ inelastic neutron scattering and their reactivity with ethylene. *Catal. Sci. Technol.* **2021**, *11* (1), 116–123.
- (33) Parker, S. F.; Lennon, D.; Albers, P. W. Vibrational Spectroscopy with Neutrons: A Review of New Directions. *Appl. Spectrosc.* **2011**, *65* (12), 1325–1341.
- (34) Parker, S. F.; Mukhopadhyay, S.; Jiménez-Ruiz, M.; Albers, P. W. Adsorbed States of Hydrogen on Platinum: A New Perspective. *Chem.—Eur. J.* **2019**, *25* (26), 6496–6499.
- (35) Kaprielova, K. M.; Yakovina, O. A.; Ovchinnikov, I. I.; Koscheev, S. V.; Lisitsyn, A. S. Preparation of platinum-on-carbon catalysts via hydrolytic deposition: Factors influencing the deposition and catalytic properties. *Appl. Catal., A* **2012**, *449*, 203–214.
- (36) Piovano, A.; Giovanni, A.; Michele, C.; Groppo, E.; Monica, J. R.; Carlo, L.; Andrea, L.; Manzoli, M.; Morandi, S.; Pellegrini, R.; Vottero, E. *Data from: Study of the Pt-hydride formation and spillover effect on Pt/Al<sub>2</sub>O<sub>3</sub> and Pt/C catalysts*; Institut Laue-Langevin (ILL), 2016, DOI: 10.5291/ILL-DATA.7-05-466.
- (37) Vottero, E.; Carosso, M.; Jimenez Ruiz, M.; Manzoli, M.; Piovano, A. *Data from: Dynamics of Pt-H species on an industrial Pt/Al<sub>2</sub>O<sub>3</sub> catalyst as a function of hydrogenation temperature*; Institut Laue-Langevin (ILL), 2021, DOI: 10.5291/ILL-DATA.7-05-514.
- (38) Ivanov, A.; Jimenez-Ruiz, M.; Kulda, J. IN1-LAGRANGE - the new ILL instrument to explore vibration dynamics of complex materials. *J. Phys.: Conf. Ser.* **2014**, *554*, 012001.
- (39) Kresse, G.; Hafner, J. Ab initio molecular-dynamics simulation of the liquid-metal-amorphous-semiconductor transition in germanium. *Phys. Rev. B* **1994**, *49* (20), 14251–14269.
- (40) Kresse, G.; Furthmüller, J. Efficient iterative schemes for ab initio total-energy calculations using a plane-wave basis set. *Phys. Rev. B* **1996**, *54* (16), 11169–11186.
- (41) Perdew, J. P.; Burke, K.; Ernzerhof, M. Generalized Gradient Approximation Made Simple. *Phys. Rev. Lett.* **1996**, *77* (18), 3865–3868.
- (42) Kresse, G.; Joubert, D. From ultrasoft pseudopotentials to the projector augmented-wave method. *Phys. Rev. B* **1999**, *59* (3), 1758–1775.
- (43) Hu, C. H.; Chizallet, C.; Mager-Maury, C.; Corral-Valero, M.; Sautet, P.; Toulhoat, H.; Raybaud, P. Modulation of catalyst particle structure upon support hydroxylation: Ab initio insights into Pd<sub>13</sub> and Pt<sub>13</sub>/γ-Al<sub>2</sub>O<sub>3</sub>. *J. Catal.* **2010**, *274* (1), 99–110.
- (44) Krokidis, X.; Raybaud, P.; Gobichon, A.-E.; Rebours, B.; Euzen, P.; Toulhoat, H. Theoretical Study of the Dehydration Process of Boehmite to γ-Alumina. *J. Phys. Chem. B* **2001**, *105* (22), 5121–5130.
- (45) Digne, M.; Sautet, P.; Raybaud, P.; Euzen, P.; Toulhoat, H. Hydroxyl Groups on γ-Alumina Surfaces: A DFT Study. *J. Catal.* **2002**, *211* (1), 1–5.
- (46) Digne, M.; Sautet, P.; Raybaud, P.; Euzen, P.; Toulhoat, H. Use of DFT to achieve a rational understanding of acid-basic properties of γ-alumina surfaces. *J. Catal.* **2004**, *226* (1), 54–68.
- (47) Ramirez-Cuesta, A. J. aCLIMAX 4.0.1, The new version of the software for analyzing and interpreting INS spectra. *Comput. Phys. Commun.* **2004**, *157* (3), 226–238.
- (48) Vottero, E.; Carosso, M.; Jiménez-Ruiz, M.; Pellegrini, R.; Groppo, E.; Piovano, A. How do the graphenic domains terminate in activated carbons and carbon-supported metal catalysts? *Carbon* **2020**, *169*, 357–369.
- (49) McInroy, A. R.; Lundie, D. T.; Winfield, J. M.; Dudman, C. C.; Jones, P.; Parker, S. F.; Lennon, D. The interaction of alumina with HCl: An infrared spectroscopy, temperature-programmed desorption and inelastic neutron scattering study. *J. Catal.* **2006**, *114* (4), 403–411.
- (50) Lagauche, M.; Larmier, K.; Jolimaitre, E.; Barthelet, K.; Chizallet, C.; Favregeon, L.; Pijolat, M. Thermodynamic Characterization of the Hydroxyl Group on the γ-Alumina Surface by the Energy Distribution Function. *J. Phys. Chem. C* **2017**, *121* (31), 16770–16782.
- (51) Albers, P. W.; Pietsch, J.; Krauter, J.; Parker, S. F. Investigations of activated carbon catalyst supports from different natural sources. *Phys. Chem. Chem. Phys.* **2003**, *5* (9), 1941–1949.
- (52) Zemlyanov, D. Y.; Smirnov, M. Y.; Gorodetskii, V. V. HREELS characterization of hydrogen adsorption states on the Pt(100)-(hex) and (1 × 1) surfaces. *Catal. Lett.* **1997**, *43* (3), 181–187.
- (53) Olsen, R. A.; Kroes, G. J.; Baerends, E. J. Atomic and molecular hydrogen interacting with Pt(111). *J. Chem. Phys.* **1999**, *111* (24), 11155–11163.
- (54) Karim, W.; Spreafico, C.; Kleibert, A.; Gobrecht, J.; VandeVondele, J.; Ekinici, Y.; van Bokhoven, J. A. Catalyst support effects on hydrogen spillover. *Nature* **2017**, *541* (7635), 68–71.
- (55) Spreafico, C.; Karim, W.; Ekinici, Y.; van Bokhoven, J. A.; VandeVondele, J. Hydrogen Adsorption on Nanosized Platinum and Dynamics of Spillover onto Alumina and Titania. *J. Phys. Chem. C* **2017**, *121* (33), 17862–17872.
- (56) Arrouvel, C.; Toulhoat, H.; Breysse, M.; Raybaud, P. Effects of PH<sub>2</sub>O, PH<sub>2</sub>S, PH<sub>2</sub> on the surface properties of anatase-TiO<sub>2</sub> and γ-Al<sub>2</sub>O<sub>3</sub>: a DFT study. *J. Catal.* **2004**, *226* (2), 260–272.
- (57) Pigeon, T.; Chizallet, C.; Raybaud, P. Revisiting γ-alumina surface models through the topotactic transformation of boehmite surfaces. *J. Catal.* **2022**, *405*, 140–151.
- (58) Wischert, R.; Laurent, P.; Copéret, C.; Delbecq, F.; Sautet, P. γ-Alumina: The Essential and Unexpected Role of Water for the Structure, Stability, and Reactivity of “Defect” Sites. *J. Am. Chem. Soc.* **2012**, *134* (35), 14430–14449.
- (59) Batista, A. T. F.; Wisser, D.; Pigeon, T.; Gajan, D.; Diehl, F.; Rivallan, M.; Catita, L.; Gay, A.-S.; Lesage, A.; Chizallet, C.; Raybaud, P. Beyond γ-Al<sub>2</sub>O<sub>3</sub> crystallite surfaces: The hidden features of edges revealed by solid-state <sup>1</sup>H NMR and DFT calculations. *J. Catal.* **2019**, *378*, 140–143.